M. Mirzaei, J. Machac, P. Ripka, A. Chirtsov, J. Vyhnanek, and V. Grim: Design of a Flat Type Magnetic Position Sensor Using Finite Difference Method accepted for IET Science, Measurement & Technology, doi 10.1049/iet-smt.2019.0197 PREPRINT

Design of a Flat Type Magnetic Position Sensor Using Finite Difference Method

Mehran Mirzaei*, Jan Machac, Pavel Ripka, Andrey Chirtsov, Jan Vyhnanek, Vaclav Grim

Faculty of Electrical Engineering, Czech Technical University, Prague 16627, Czech Republic
*mirzameh@fel.cvut.cz

Abstract: This paper presents an analysis and the design of a new flat-type position sensor with an external armature. One excitation coil and two antiserially connected pick-up coils are used in the stationary part. Solid iron segments or steel lamination segments are used for the moving armature. The proposed position sensor was modelled using linear movement. A 2D finite difference method (FDM) was developed and was used for fast analysis for optimizing the sensor. The induced eddy currents in the solid armature were taken into account in the finite difference analysis. The finite difference calculations were compared with 2-D and 3-D FEM simulations and with experimental results. The sensor has a total error of 0.23 mm rms for 36 mm range without any compensation. Unlike previous designs, our new sensor has no moving coil.

Nomenclature

A_z	z-axis component of the magnetic vector potential
f	frequency
μ	magnetic permeability = $\mu_r\mu_0$
σ	electrical conductivity
J_s	source current density
R	μ_m/μ_n
μ_m	relative magnetic permeability of region m
μ_n	relative magnetic permeability of region n
w_c	coils width
h_c	coils height
d_p	excitation coil inner distance
d_e	pick up coil inner distance
t	distance between coils sides
w_i	armature width
h_i	armature iron height
g	distance between coils and armature
L	square box edge length for boundary conditions
$\mu_{r\text{-}i}$	initial relative magnetic permeability of the
σ_i	armature
M	electrical conductivity of the armature
Ψ	mutual inductance between coils
V	mutual flux linkage between coils
X	induced voltage in the pick-up coils
N	armature position
I	number of turns of the pick up and excitation coils
L_i	current amplitude
	armature width in the z-direction

1. Introduction

The linear variable differential transformer (LVDT) is a very popular magnetic position sensor because of its non-contact nature and its high precision [1]. Because of its simple and robust structure it is suitable for industrial applications. The conventional LVDT sensor is cylindrical in shape with an axially-symmetric configuration [2]-[4]. A flat shape LVDT is more suitable for harsh environments, because the stationary parts and the moving parts (the armature) can be completely physically isolated, unlike in the case of the cylindrical LVDT [5]-[10]. LVDT sensors can be constructed with an armature (magnetic core) [2]-[3] and [7]-[8], or can be coreless [4]-[6] and [9]-[10]. Despite its high brittleness, ferrite is a widely-used material for LVDT sensors with magnetic cores. LVDT sensors with nickel iron and cobalt iron alloys show enhanced performance, but these alloys are more expensive [11]. The influences of magnetic materials must be taken into account in the design of position sensors [11]-[12]. A cylindrical LVDT is usually highly immune to interference e.g. from movements of ferromagnetic objects in the close vicinity. It often even has magnetic shielding around the coil.

However, for some installations the flat design of the LVDT is required with physically separated stationary and moving parts. An example of such an application is an elevator cabin landing position sensor, which may have a single armature connected to the cabin and one coil system in each floor. Magnetic sensors would be better resistant to dust and oil than the optical sensors which are currently used for this application. A flat type coreless LVDT sensor was presented in [5]-[6] and in [9]-[10], with a moving excitation coil or pick-up coils. This solution with moving coils is impractical, and sensors with a large stroke suffer from low reliability.

We address this problem by introducing a novel type of flat LVDT sensor with an external armature made of solid iron and steel lamination. The advantage of this design compared to existing solutions is the absence of a moving coil, and thus high robustness and reliability. A 2D finite difference method (FDM) [13]-[14] description has been developed for a flat type LVDT sensor, taking into account the eddy currents in the armature [15]-[16]. The design of the position sensor could be optimized by using the FDM presented here to provide improved precision and performance [17]-[19]. The 3D finite element method (FEM) was also used to evaluate third dimension effects on the flat type position sensor [20]. The main purpose of this paper is to present the design and an analysis of a new flat type position sensor with a solid iron armature using fast and precise FDM. For the purposes of comparison, a steel lamination armature is also used to evaluate the material effects. We compare the efficiency and the precision of the 2D FDM model with 2D and 3D FEM models. The modelling results are verified by measurements on the sensor demonstrator. We limit our analysis to a simple sensor with antiserially connected pick-up coils. We do not take into

consideration the shielding against external DC fields that also suppresses the influence of nearby ferromagnetic bodies.

2. Model

Fig. 1 shows the flat LVDT sensor and its equivalent electric circuit. The magnetic shield or yoke is not considered in this paper. The performance of an LVDT sensor is similar to the performance of a transformer with an open circuit secondary coil. The primary coil and the secondary coils are the excitation coil and the pick-up coils in the LVDT sensor, respectively. The pick-up coils are connected in series anti-phase (antiserial), which gives zero output voltage for the null (centre) position of the armature.

3. Finite Difference Method (FDM)

The general partial differential equation in the 2D *x-y* plane using Maxwell equations is as follows [16]:

$$\frac{\partial^2 A_z}{\partial x^2}+\frac{\partial^2 A_z}{\partial y^2}-j\omega\mu\sigma A_z+\mu J_s=0 \qquad (1)$$

$$\omega=2\pi f$$

Only linear magnetic modelling using the initial permeability is considered here, due to the low magnetic fields in the sensor, and nonlinearity and hysteresis effects are neglected. Third term in (1) is zero for nonconductive (no eddy current effects) coils and air regions. Fourth term in (1) is zero in armature and air regions. Fig. 2 shows a schematic finite difference meshed model for two regions m (gray color) and n (white color), and a 5-node finite difference mesh element. The two adjacent regions m and n could have a common edge or common vertices at the corners and boundaries. Parameters $p{\cdot}h$, $q{\cdot}h$, $r{\cdot}h$ and $s{\cdot}h$ are the mesh dimensions in the *x* and *y* directions in Fig. 2 (b). The finite difference equation of (1) for either region m or region n is presented in (2), using Taylor expansions [14]:

$$\frac{A_{z,1}}{p\cdot(p+r)}+\frac{A_{z,2}}{q\cdot(q+s)}+\frac{A_{z,3}}{r\cdot(p+r)}+\frac{A_{z,4}}{s\cdot(q+s)} \qquad (2)$$
$$-\left(\left(\frac{1}{p\cdot r}+\frac{1}{q\cdot s}\right)+j\omega\mu\sigma\cdot\frac{h^2}{2}\right)\cdot A_{z,0}+\mu J_s\cdot\frac{h^2}{2}=0$$

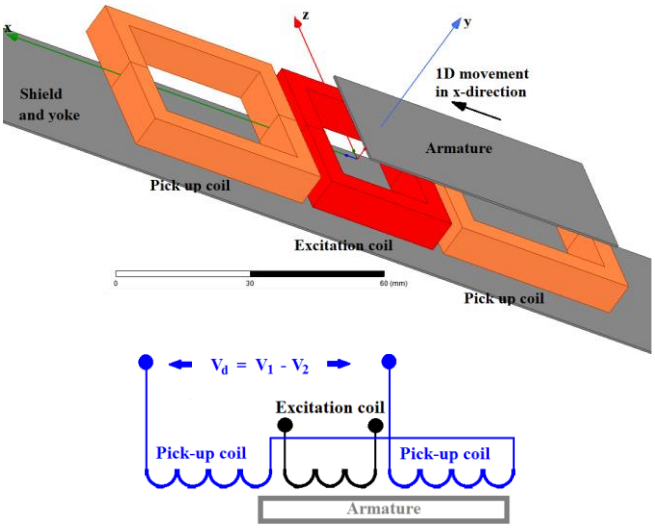

Fig. 1. *(a) Flat type position sensor with a magnetic armature (top) and (b) its equivalent electric circuit model (bottom)*

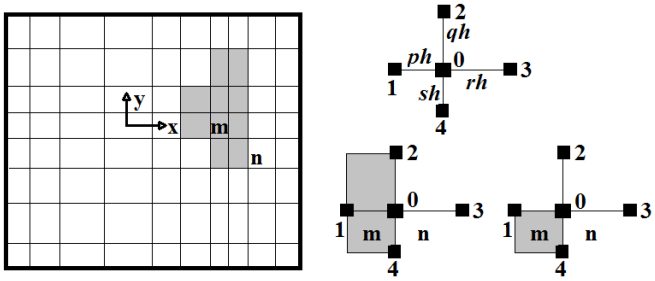

Fig. 2. *(a) Schematic model of finite difference meshed elements for adjacent regions m and n (left) and (b) for a finite difference mesh element (right) - region m with gray color is surrounded by region n with white color*

The centre point 0 in the element has magnetic vector potential $A_{z,0}$, and the magnetic vector potential at nearby node 1 is $A_{z,1}$, at node 2 the magnetic vector potential is $A_{z,2}$, at node 3 it is $A_{z,3}$, and at node 4 it is $A_{z,4}$. Equation (3) presents the finite difference equation when node 0 with magnetic vector potential $A_{z,0}$ is on the boundary edge between regions m and n [15]-[16]:

$$\frac{A_{z,1}}{p}+\frac{(p\cdot R+r)}{q\cdot(q+s)}\cdot A_{z,2}+\frac{R}{r}\cdot A_{z,3}+\frac{(p\cdot R+r)}{q\cdot(q+s)}\cdot A_{z,4}$$
$$-\left(\left(\frac{1}{p\cdot r}+\frac{1}{q\cdot s}\right)\cdot(p\cdot R+r)+j\omega\mu\sigma\cdot p\cdot\frac{h^2}{2}\right)\cdot A_{z,0} \qquad (3)$$
$$+\mu J_s\cdot p\cdot\frac{h^2}{2}=0$$

$$R=\frac{\mu_m}{\mu_n}$$

Equations (2) and (3) can be simplified further when the mesh element has the same sizes for the element edges (p=q=r=s=1), which are presented in (4) and (5), respectively.

$$A_{z,1}+A_{z,2}+A_{z,3}+A_{z,4}-\left(4+j\omega\mu\sigma\cdot h^2\right)\cdot A_{z,0} \qquad (4)$$
$$+\mu J_s\cdot h^2=0$$

$$A_{z,1}+\frac{(R+1)}{2}\cdot A_{z,2}+R\cdot A_{z,3}+\frac{(R+1)}{2}\cdot A_{z,4} \qquad (5)$$
$$-\left(2\cdot(R+1)+j\omega\mu\sigma\cdot\frac{h^2}{2}\right)\cdot A_{z,0}+\mu J_s\cdot\frac{h^2}{2}=0$$

The finite difference equation for a node on the corner located on the boundary between regions m and n is [14]-[16]:

$$\frac{(R+1)}{2}\cdot A_{z,1}+R\cdot A_{z,2}+R\cdot A_{z,3}+\frac{(R+1)}{2}\cdot A_{z,4} \qquad (6)$$
$$-\left(3\cdot R+1+j\omega\mu\sigma\cdot\frac{h^2}{4}\right)\cdot A_{z,0}+\mu J_s\cdot\frac{h^2}{4}=0$$

It is considered that region m contains the source current, and it is the conductive region in (3), (5) and (6) [15]-[16].

Fig. 3 presents a computational model for a flat type position sensor for FDM modelling.

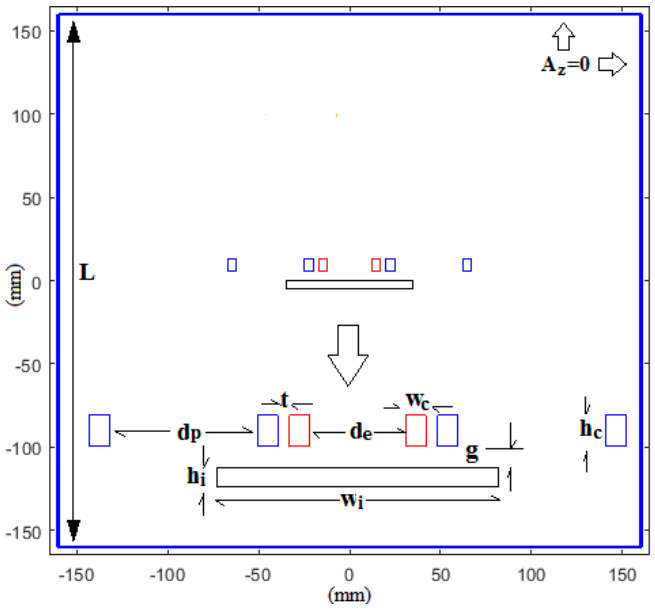

Fig. 3. *Computational model for finite difference analysis of a flat type position sensor with boundary conditions*

The solution space is limited to ± 160 mm and that condition $A_z = 0$ is applied at the solution space boundary (Fig. 3). The magnetic flux densities are calculated at the centre point of each element inside any region in (7), using the approximations in (8):

$$B_{x,0} = \frac{\partial A_z}{\partial y} = \frac{A_{z,2} - A_{z,4}}{h \cdot (q+s)} \tag{7}$$

$$B_{y,0} = -\frac{\partial A_z}{\partial x} = \frac{A_{z,1} - A_{z,3}}{h \cdot (p+r)}$$

$$A_{z,0} = \frac{s \cdot A_{z,2} + q \cdot A_{z,4}}{q+s} \rightarrow (B_{x,0}) \tag{8}$$

$$A_{z,0} = \frac{r \cdot A_{z,1} + p \cdot A_{z,3}}{p+r} \rightarrow (B_{y,0})$$

The magnetic flux densities at the common edge boundary, and the common corner boundaries between regions m and n, for example in Fig. 2 (b), could be approximately written as in (9) and (10), respectively.

$$B_{x,0} = \frac{A_{z,2} - A_{z,4}}{h \cdot (q+s)} \tag{9}$$

$$B_{y,0} = 0.5 \cdot \left(\frac{A_{z,1} - A_{z,0}}{h \cdot p} + \frac{A_{z,0} - A_{z,3}}{h \cdot r} \right)$$

$$B_{x,0} = 0.5 \cdot \left(\frac{A_{z,2} - A_{z,0}}{h \cdot q} + \frac{A_{z,0} - A_{z,4}}{h \cdot s} \right) \tag{10}$$

$$B_{y,0} = 0.5 \cdot \left(\frac{A_{z,1} - A_{z,0}}{h \cdot p} + \frac{A_{z,0} - A_{z,3}}{h \cdot r} \right)$$

Fig. 2 shows a simplified FDM mesh model to explain the finite difference method used in this paper. Each node is adjacent to 4 nodes, which is totally 5 nodes for each mesh inside the model, except the nodes on the boundary with determined zero magnetic vector potential. Each node can be inside a region or on the boundary between different regions, as shown in Fig. 2.

4. FDM Simulations

Table 1 presents flat type position sensor dimensions and properties. The other dimensions are defined in Fig. 3. The initial relative magnetic permeability $\mu_{r\text{-}i}$ (which is 100 for solid iron and 1000 for steel lamination) and the electrical conductivity σ_i of the solid iron and steel lamination armature are also presented in Table 1. The initial permeability is used because the magnetic fields in the position sensor are very small.

Table 1 Flat type position sensor parameters

Parameter	Value
N	70
I	0.165 A
L	320 mm
w_c	5 mm
h_c	8 mm
w_i	50 mm and 70 mm
h_i	5 mm and 0.5 mm
d_e	24 mm
d_p	37 mm
g	5.4 mm
t	3 mm
σ_i	5.07 MS/m, 3.14 MS/m
$\mu_{r\text{-}i}$	100 and 1000
L_i	30 mm

Two source frequencies, 50 Hz and 400 Hz, were selected for the first analysis of the flat type position sensor. The corresponding skin depths for solid iron are calculated for the mesh size at these frequencies, using the following equation [1]:

$$\delta_i = \sqrt{\frac{2}{\omega \mu_{r-i} \mu_0 \sigma_i}} \tag{11}$$

The skin depths are 3.2 mm at 50 Hz, and 1.1 mm at 400 Hz.

Fig. 4 and Fig. 5 show the magnetic flux distribution. The length of square box L for the boundary conditions is considered to be 320 mm, which is a satisfactory value for precision and speed of simulation. The effect of the induced eddy current in the solid iron armature is obvious at 400 Hz (Fig. 5). Fig. 6 and Fig. 7 present the magnetic flux distribution for different heights of the solid iron armature and for different coils and armature gap g, in order to evaluate the sensitivity and the performance of the magnetic position sensor.

Fig. 8 presents the magnetic vector potential versus distance on the line in the middle of the coils. The difference between the DC and 50 Hz values is negligible, while the magnetic vector potential results vary considerably and are reduced on one side at 400 Hz. The x component of the magnetic flux density curve at 1 mm below the surface of the moving iron part is presented in Fig. 9. The field values are in the mT range, which confirms the use of the constant initial relative magnetic permeability in the magnetic modelling. Only AC models are used for the design of the position sensor, as there is no induction component at DC.

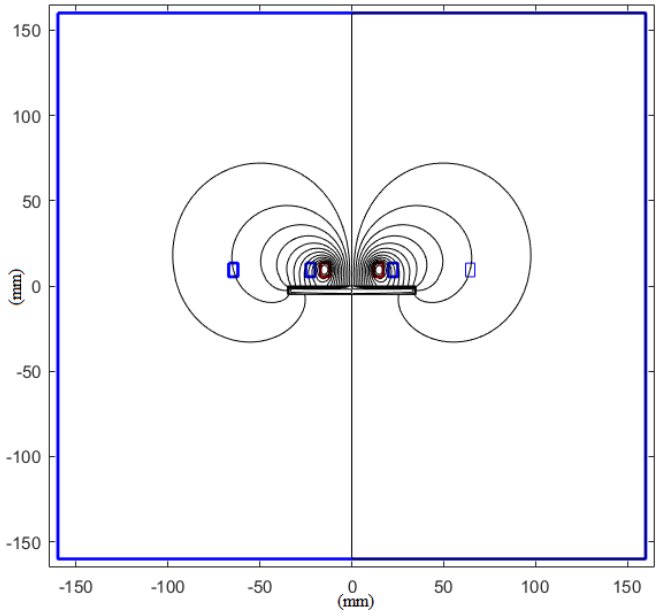

Fig. 4. *Magnetic flux distribution at 400 Hz with zero position armature - solid iron armature width and height = 70 mm and 5 mm (the boundary edge is 320 mm in length)*

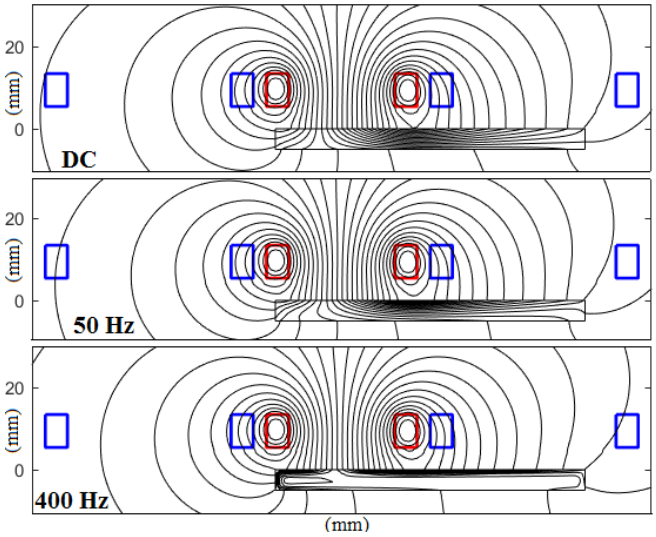

Fig. 5. *Magnetic flux distribution at DC (top), at 50 Hz (middle), and at 400 Hz (bottom) - solid iron armature shifted 20 mm from centre (armature width= 70 mm and height mm =5 mm)*

The centre position for the armature is that vertical symmetry lines of the coils and the armature align (Fig. 4). The relations between the magnetic vector potential and induced voltage V and mutual inductance M are [21]:

$$V = -\frac{d\Psi}{dt} = -j\omega N \oint A_z dl \qquad (12\ a)$$

$$M = \frac{-N \oint A_z dl}{I} \qquad (12\ b)$$

where Ψ is the mutual flux linkage between the excitation coil and the pick-up coils.

The induced voltage V in the pick-up coils and the mutual inductance M between the excitation coil and the pick-up coils are particularly influenced by the induced eddy current in the solid iron at higher frequencies.

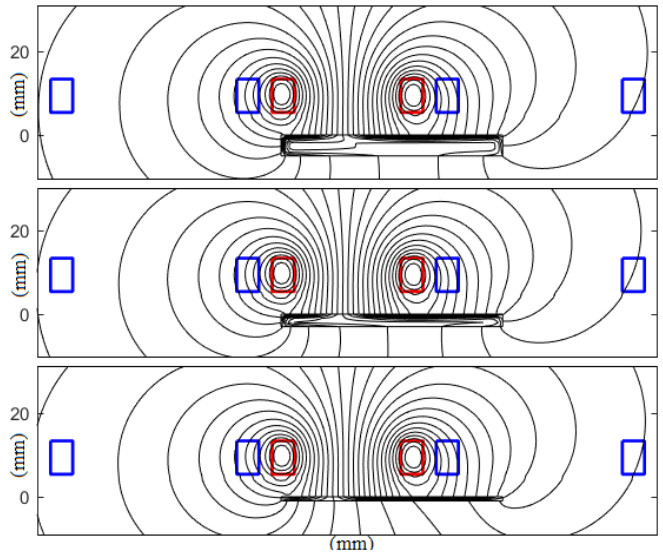

Fig. 6. *Magnetic flux distribution at 400 Hz for solid iron armature height = 5mm (top), 3 mm (middle) and 1 mm (bottom) – Armature shifted 10 mm from centre (armature width = 50 mm)*

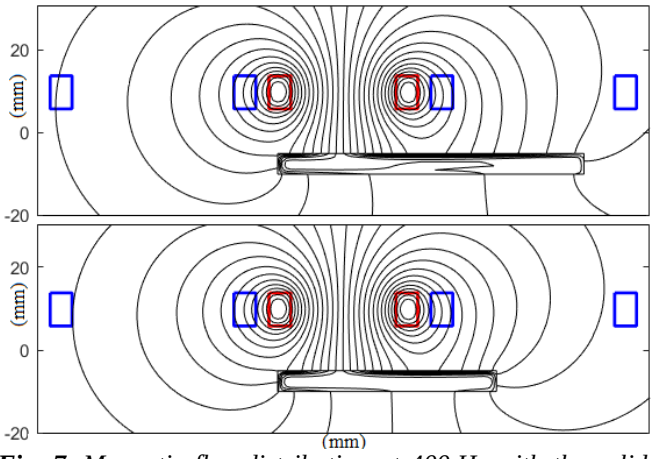

Fig. 7. *Magnetic flux distribution at 400 Hz with the solid iron armature shifted 20 mm from centre and armature width = 70 mm (top) and the armature shifted 10 mm from centre and armature width = 50 mm (bottom) – the gap between the coils and the armature, g, is doubled, and is equal to 10.8 mm*

The induced voltage V and the mutual inductance M are numerically calculated from the relations:

$$V = -j\omega N L_i \frac{\sum_{k=1,2,\cdots}^{K} \left(A_{z,k}^{l} - A_{z,k}^{r}\right)}{K} \qquad (13\ a)$$

$$M = \frac{-NL_i}{I} \frac{\sum_{k=1,2,\cdots}^{K} \left(A_{z,k}^{l} - A_{z,k}^{r}\right)}{K} \qquad (13\ b)$$

The equations (13 a) and (13 b) are calculated using (12 a) and (12 b) for FDM by averaging on the coil sides cross section and subtracting the left (l) and the right (r) of the coil sides [21]. The integral path in (12 a) and (12 b) is only in the z direction, as only the z component of the magnet vector potential A_z is considered in 2D FDM analysis (Fig. 10). Parameter K is the number of nodes of FDM on the cross section of the coil sides.

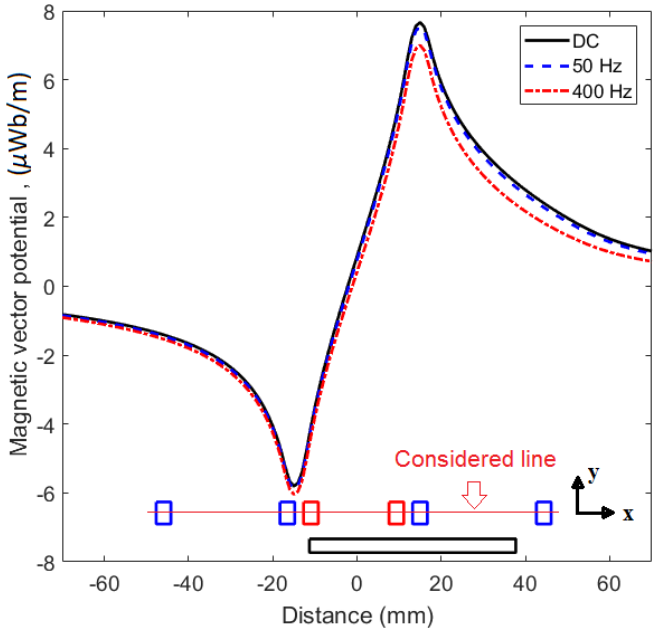

Fig. 8. *Real part of the magnetic vector potential versus distance on the red line in the middle of the coils –solid iron armature 70 mm width and 5 mm height (armature shifted 20 mm from centre).*

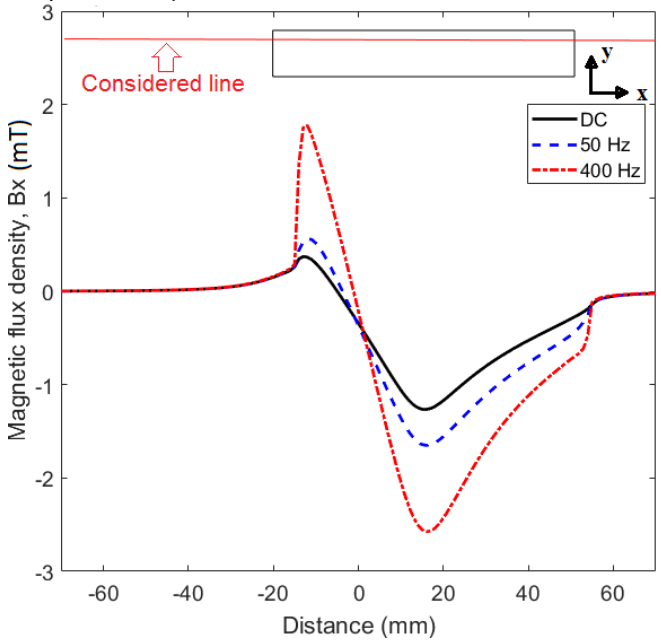

Fig. 9. *Real part of x component of magnetic flux density versus distance on the red line 1 mm below the surface of the armature - solid iron armature 70 mm width and 5 mm height (armature shifted 20 mm from centre)*

Mutual inductances with different armature widths and heights are presented in Table 2, for DC and 400 Hz for the zero position of the armature. The width of the armature has a substantial effect on mutual inductance *M*. A change in the height of the armature from 5 mm to 3 mm gives 1% less influence on the mutual inductance. However, the mutual inductance decreases by about 5% for 1 mm height. A larger gap *g* causes less influence of the height and the width of the armature on the mutual inductances. Increasing gap from 5.4 mm to 10.8 mm has larger influence than other parameters.

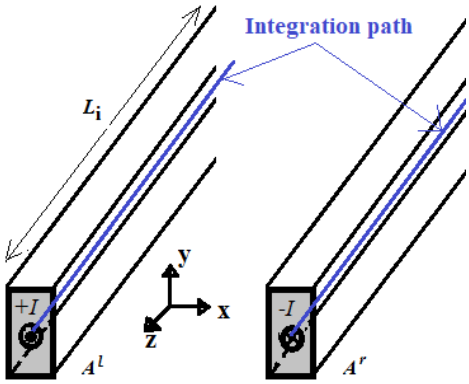

Fig. 10 . *Coil model with coil sides In (A^r) and Out (A^l) of pl*

Table 2 Mutual inductance between the excitation coil and the pick-up coil at zero position of the armature

	Height	Width	Inductance	Gap, *g*
DC	5 mm	70 mm	43.5 μH	5.4 mm
400 Hz			41.3 μH	
DC	3 mm	70 mm	43.1 μH	5.4 mm
400 Hz			41.3 μH	
DC	1 mm	70 mm	41.4 μH	5.4 mm
400 Hz			41.1 μH	
DC	5 mm	50 mm	39.0 μH	5.4 mm
400 Hz			37.6 μH	
DC	3 mm	50 mm	38.6 μH	5.4 mm
400 Hz			37.4 μH	
DC	1 mm	50 mm	37.4 μH	5.4 mm
400 Hz			37.3 μH	
DC	5 mm	70 mm	37.0 μH	10.8 mm
400 Hz			36.0 μH	
DC	1 mm	70 mm	36.0 μH	10.8 mm
400 Hz			35.9 μH	
DC	5 mm	50 mm	34.7 μH	10.8 mm
400 Hz			34.1 μH	

The influence of the induced eddy current in the solid iron armature on the mutual inductance is evident in a comparison between 400 Hz and DC. Reducing the height of the armature has less influence on the mutual inductance at 400 Hz independent of gap values, *g* because skin depth is smaller and the magnetic flux is concentrated on the surface of the solid iron armature. This can be used for applications measuring the positions of changing targets.

The induced eddy current in the armature causes the self inductance of excitation coil and mutual inductances between excitation coil and pick up coils to be complex value. It can be explained that phase angle shift between flux linkage and excitation coil current is nonzero or phase angle shift between induced voltage and excitation coil current is not any longer 90 Deg. Therefore, the inductance values calculated by (13 b) are complex numbers, because of the induced eddy currents in the solid iron armature.

The mutual inductances between the excitation coil and the pick-up coils for the right (*M*1) and left (*M*2) pick-up coils and their difference, *M*1-*M*2 (differential inductance) versus the positions of the armature, are shown in Fig. 11 and Fig. 12, which are almost sinusoidal in shape [22]. Only the real parts are shown, and the imaginary part of the mutual inductance is not considered as in Table 2. The differential inductances change linearly from the zero position of the armature to close to maximum values.

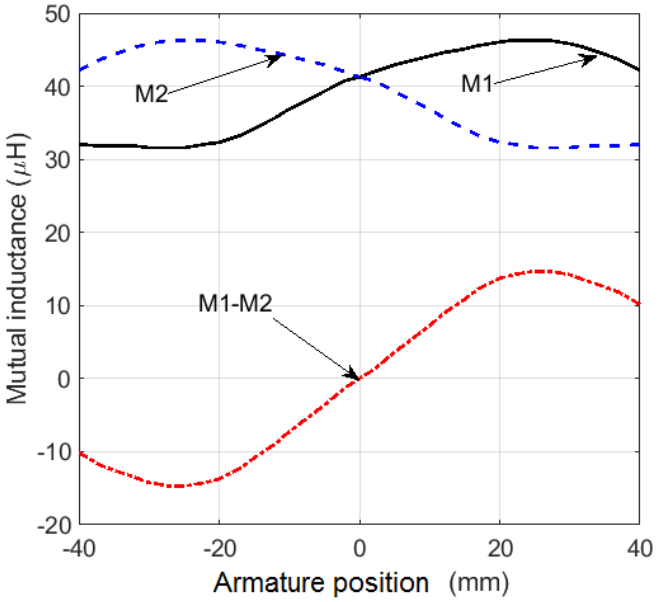

Fig. 11. *Mutual inductance versus armature position – the solid iron armature is 70 mm in width (400 Hz)-FDM*

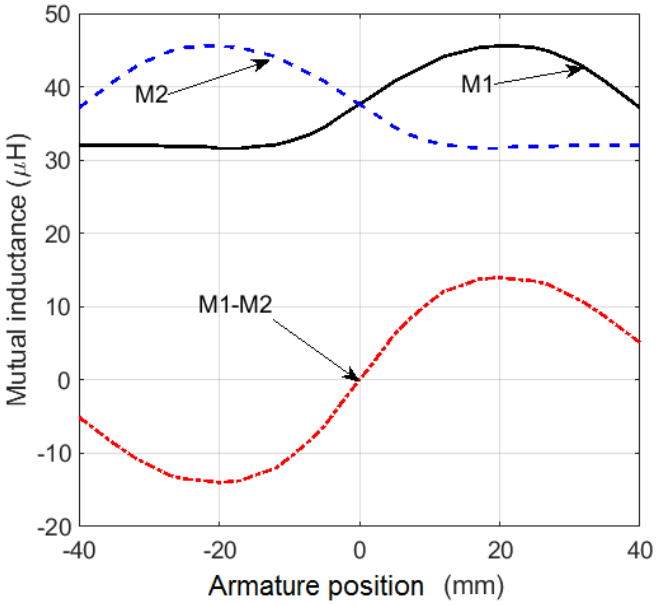

Fig. 12. *Mutual inductance versus armature position – the solid iron armature is 50 mm in width (400 Hz)-FDM*

They are odd symmetric functions relative to the zero position. The gradient of the differential inductance curve is higher for an armature 50 mm in width than for an armature 70 mm in width. The maximum differential inductance values are about 14 μH, at 25 mm and 20 mm for armatures of 70 mm and 50mm length, respectively.

5. Experimental results

Fig. 13 shows experimental elements, coils and armatures, and also the Stanford Research SR 830 lock-in amplifier and the Keithley 3390 signal generator. The armatures are of solid iron 5 mm in thickness and electrical steel 0.5 mm in thickness.

The experimental results and the FDM results for the differential voltage amplitudes of the pick-up coils for the solid iron armatures are presented in Fig. 14, for 400 Hz, and in Fig. 15 for 50 Hz. The polarity of the differential voltages is determined on the basis of the phase angles. They contain both inductive and resistive components.

The linear region of the differential voltage curves is used for the magnetic position sensor. The magnetic sensor shows better sensitivity or higher voltage at a smaller distance with the 50 mm armature, and better sensitivity at a longer distance with the 70 mm armature in the linear region of the curves. The maximum values of the differential voltages are located at the same position as the maximum values of the differential mutual inductances curves, *M*1-*M*2 in Figs. 11 and 12. In addition, Fig. 16 and Fig. 17 show the differential voltages for an armature of steel laminations. The maximum values are higher, especially at higher frequencies, due to the higher initial permeability, 1000, and the smaller height (Fig. 18). The main sources of the differences between the experimental results and the FDM results for differential voltages are the effects of the third dimension, which are not taken into account in the 2D finite difference analysis.

6. Numerical analysis evaluations

Table 3 shows comparisons between FDM results, 2D FEM calculations and 3D FEM calculations [20] for differential voltages for different positions of a solid iron armature 70 mm in width. The 3D FEM results agree better with the experimental results, because 3D FEM takes into account the third dimension effect, which is not negligible for rectangular coil fields [23] in a magnetic position sensor. The 2D FDM and 2D FEM results are both higher than the experimental results and the 3D FEM results. Taking 3D effects into account reduces the differential voltages and the corresponding mutual inductances between the exciting coil and the pick-up coils. The 2D FDM calculations that have been developed agree well with 2D FEM at 50 Hz.

Reducing the height of the armature reduces the high-frequency effects of the induced eddy currents in the solid iron (see Fig. 19). The results for differential voltage with and without taking into account the electrical conductivity of the armature show small differences for a solid iron armature 1 mm in height. The maximum value of the differential voltage for a solid iron armature 1 mm in height is almost unchanged in comparison with a solid iron armature 5 mm in height at 400 Hz (Fig. 14).

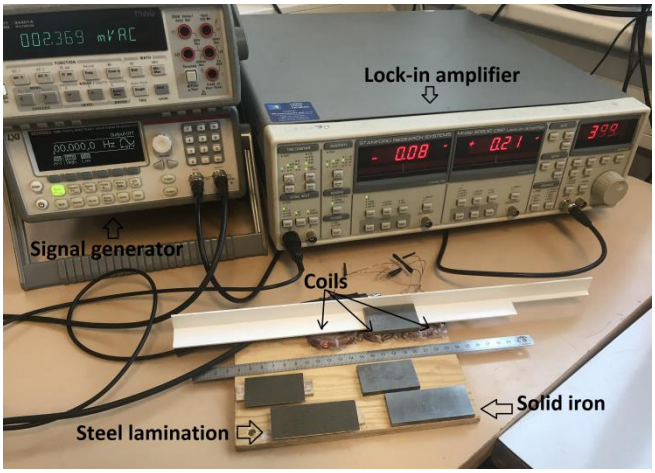

Fig. 13. *Experiment elements - coils and solid iron and steel lamination armatures – Lock-in amplifier and signal generator*

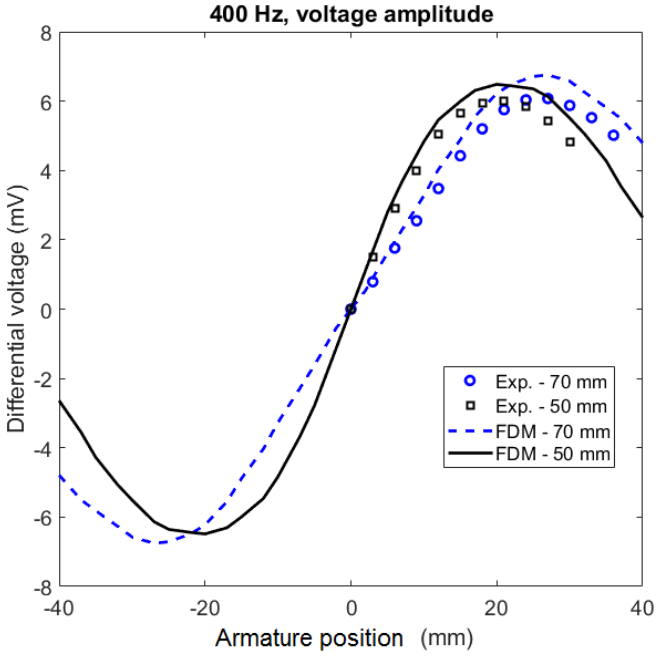

Fig. 14. *Differential voltage versus solid iron armature position - 400 Hz (experimental versus FDM)*

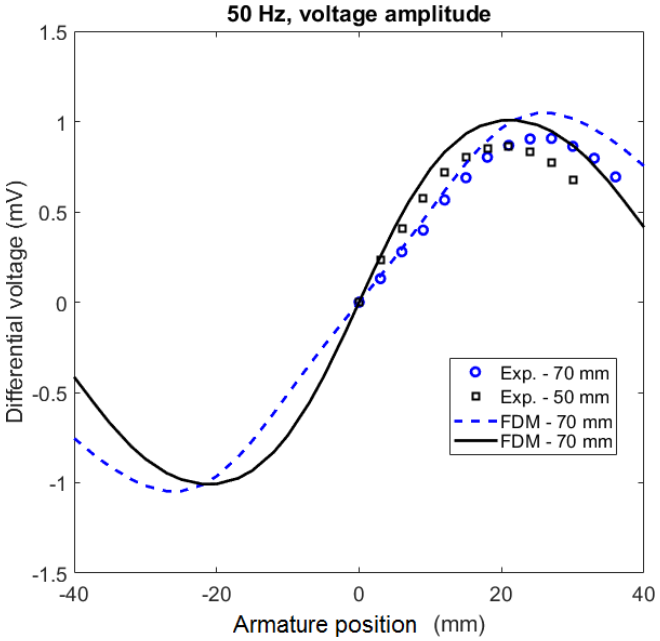

Fig. 15. *Differential voltage versus solid iron armature position - 50 Hz (experimental versus FDM)*

Table 3 Differential voltage versus solid iron armature position at 50 Hz - comparison between experimental, FDM, FEM 2D and FEM 3D

Position (mm)	Exp. (mV)	FDM (mV)	FEM 2D (mV)	FEM 3D (mV)
9	0.40	0.45	0.46	0.42
18	0.80	0.90	0.89	0.80
27	0.91	1.04	1.04	0.90

7. Linearity

A linear approximation of the relation between differential voltage V and armature position X is:

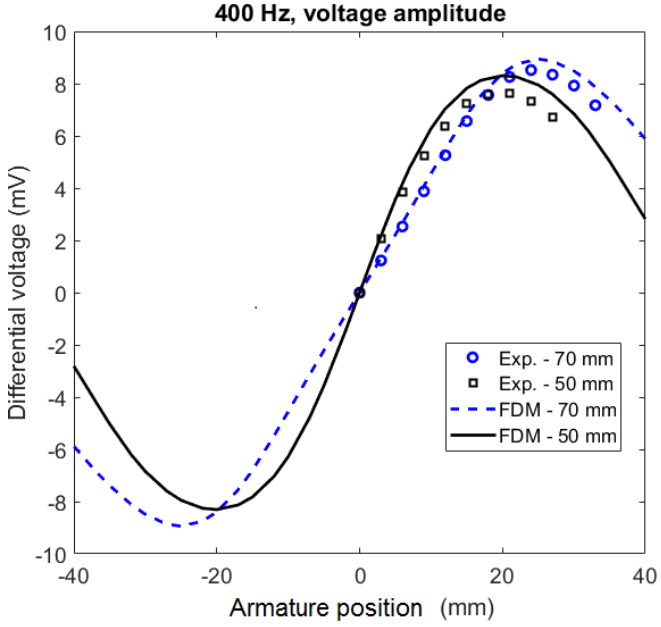

Fig. 16. *Differential voltage versus steel lamination armature position - 400 Hz (experimental versus FDM)*

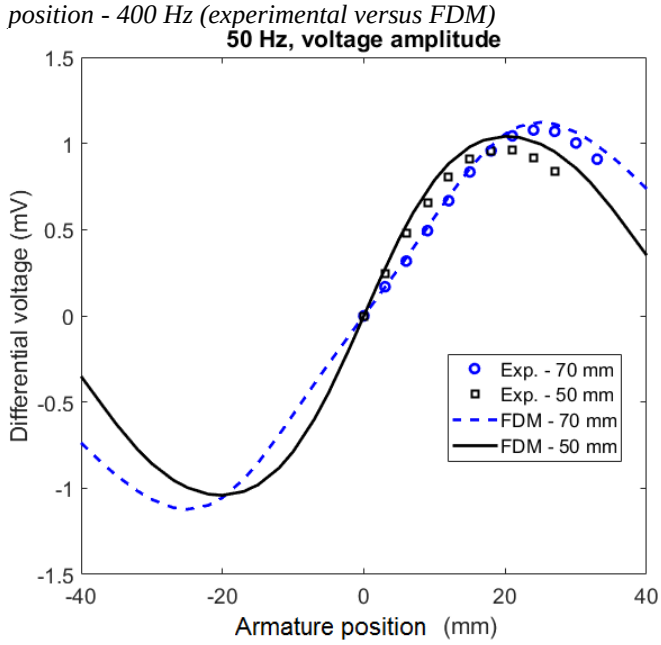

Fig. 17. *Differential voltage versus steel lamination armature position - 50 Hz (experimental versus FDM)*

$$X = C \cdot V \tag{14}$$

Constant C depends on the width of the armature and the frequency of the excitation coil (Table 4). Table 5 presents root mean square error (RMSE) values as an indicator [12] to show the closeness of the Q measured values to the linear curve fit in (14).

Table 4 Constant C for various solid iron (SI) and steel lamination (SL) armature widths and frequencies

	70 mm 400 Hz	70 mm 50 Hz	50 mm 400 Hz	50 mm 50 Hz
C, SI (mm/mV)	3.4	22	2.3	16
C, SL (mm/mV)	2.3	18	1.8	14

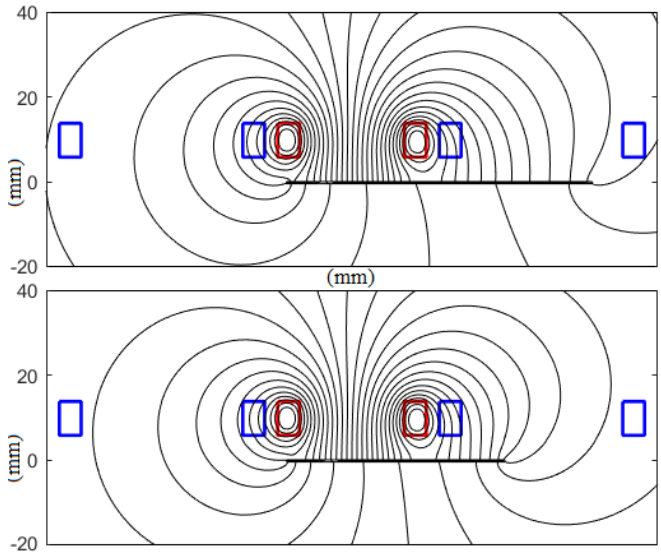

Fig. 18. *Magnetic flux distribution at 50 Hz with the steel lamination armature shifted 20 mm from centre and armature width = 70 mm (top) and with the armature shifted 10 mm from centre and armature width = 50 mm (bottom) – The gap between the coils and the armature is 5.4 mm*

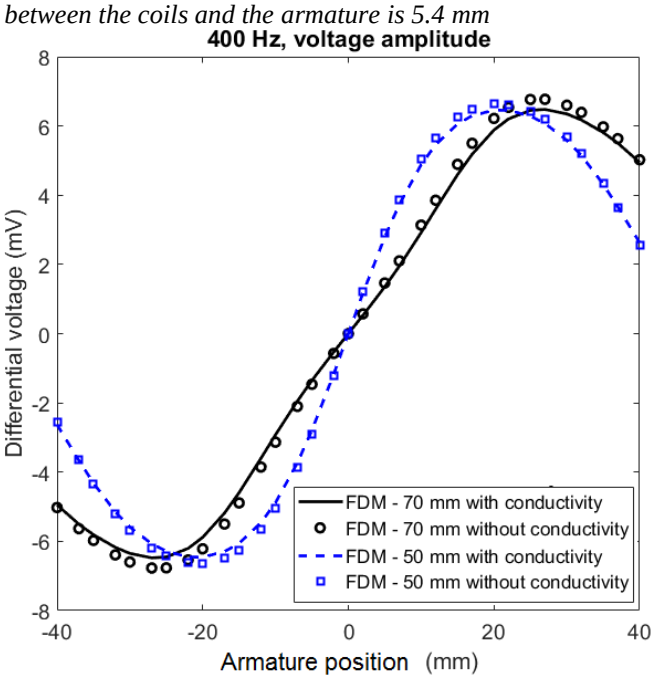

Fig. 19. *Differential voltage versus solid iron armature position with a moving part 1 mm in height (FDM)*

The linear ranges considered here are -12 mm to +12 mm for an armature 50 mm in width and -18 mm to +18 mm for an armature 70 mm in width. Reducing the manufacturing tolerance of the magnetic sensor and induced eddy currents in the solid iron could reduce the root mean square error in Table 5.

Table 5 RMSE for various solid iron (SI) and steel lamination (SL) armature widths and frequencies

	70 mm 400 Hz	70 mm 50 Hz	50 mm 400 Hz	50 mm 50 Hz
RMSE, SI (mm)	0.23	0.26	0.43	0.48
RMSE, SL (mm)	0.26	0.33	0.64	0.50

8. Discussion

Although non-commercial and commercial finite element softwares for 2D and 3D electromagnetic analysis for magnetic devices and sensors is highly accessible and has high precision [24]-[30], fast and sufficiently precise in-house analytical and numerical approaches to the design and optimization of electromagnetic devices [31]-[36] are always in demand in industry and in academic. Easy postprocessing of magnetic analysis, fast parametric analysis and flexible optimizations are major advantages of in-house analytical and numerical computational tools for all types of electromagnetic devices such as magnetic sensors and actuators.

3D numerical calculations are more time-consuming, as they have more unknowns to solve. 3D finite difference equations have three components of magnetic vector potential, in comparison with only one component of magnetic vector potential in the 2D finite difference method presented in this paper. It is not economical or efficient to use 3D computation in the whole design process of our sensor, as the difference between 2D simulations and 3D simulations is only 10%, as shown in Table 2.

Solid iron and steel may be a fundamental component of magnetic position sensors [24]. If this is the case, induced eddy currents should be considered. It is essential to take into consideration the magnetic permeabilities and the electrical conductivities of magnetic materials [37] in the design of magnetic position sensors.

The effects of the magnetic shield and the yoke in Fig. 1 (a) are not considered in this paper. These parts will provide improved sensitivity.

9. Conclusion

We have developed a novel flat LVDT sensor with an external armature and without moving coils. Finite difference analysis and experimental results have been presented for solid iron and electrical steel lamination armatures. Various dimensions of the armature and the gaps have been taken into account in the modelling and in experiments at two frequencies. We have verified by 3D FEM and by experiments that 2D FDM analysis is reasonably precise and reasonably fast for flat type position sensor design and optimization. Third dimension effects are noticeable, but they can be neglected in order to save simulation time in the first step in optimizing the design of a flat type magnetic position sensor.

The magnetic fields in the armature are low. It is therefore preferable to use a thin or laminated armature and to operate the sensors at high frequencies, if the application allows. A magnetic position sensor with a steel lamination armature at 400 Hz shows superior results, as the eddy currents are minimized even at 400 Hz thanks to the lamination. High operational frequency also improves the dynamic performance of the sensor. The sensor that has been developed has a total error of 0.23 mm rms for 36 mm range without any compensation for nonlinearity. This is acceptable for applications such as an elevator cabin landing position sensor. The power consumption at 50 Hz and 400 Hz is 10 mW. For the final design, the operation frequency may be further increased and the number of turns of the coils should be optimized taking into account the sensitivity and the power consumption.

The analysis presented here was limited to a simple sensor with antiserially connected pick-up coils. Advanced LVDTs often compensate temperature effects and airgap variations by more complicated processing of the sensor output. The simulation procedures presented here can also be utilized in the analysis of such schemes. Both compensations would be necessary for this practical application.

A weak point in the flat-type LVDT is its sensitivity to the movement of ferromagnetic bodies in the vicinity of the sensor. If this situation is anticipated, the FDM simulation method presented here can be used to estimate the influence on the precision of the sensor and to evaluate the efficiency of the magnetic shielding.

10. References

[1] Ripka, P.: '*Magnetic sensors and magnetometers*' (Artech House, Jan. 1, 2001)

[2] Kilani, M., Taifour, S., Al-Sharif, L.: 'Effect of design geometry on the performance characteristics of linear variable differential transformers', *Sens.& Trans.*, 2013, **150**, (3), pp. 66-71

[3] Sykulski, J. K., Sykulska, E., Hughes, S. T.: 'Application of finite element modelling in LVDT design', *Int. J. Comput. Math. Electr. Electron. Eng. COMPEL*, 1992, **11**, (1), pp. 73–76,

[4] Martino, M., Danisi, A., Losito, et al.: 'Design of a linear variable differential transformer with high rejection to external interfering magnetic field', *IEEE Trans. Mag*., 2010, **46**, (2), pp. 674 - 677

[5] Sydenham, P.H., Taing, V., Mounsey, D.J., et al.: 'Low-cost, precision, flat inductive sensor', *Measurement*, 1995, **15**, (3), pp. 179-188

[6] Kano, Y., Hasebe, S., Huang, C., et al.: 'New type linear variable differential transformer position transducer', *IEEE Trans. Instr. and Meas.*, 1989, **38**, (2), pp. 407 - 409

[7] Kano, Y., Hasebe, S., Miyaji, H.: 'New linear variable differential transformer with square coils', *IEEE Trans. Mag.*, 1990, **26**, (5), pp. 2020–2022

[8] Babu, A., and George, B.: 'Design and development of a new non-contact inductive displacement sensor', *IEEE Sens. J.*, 2018, **18**, (3), pp. 976-984

[9] Djuric, S. M.: 'Performance analysis of a planar displacement sensor with inductive spiral coils', *IEEE Trans. Mag.*, 2014, **50**, (4), pp. 1-4

[10] Anandan, N., George, B.: 'Design and development of a planar linear variable differential transformer for displacement sensing', *IEEE Sen. J.*, 2017, **17**, (16), pp. 5298-5305

[11] Yañez-Valdez, R., Alva-Gallegos, R., Caballero-Ruiz, A., et al.: 'Selection of soft magnetic core materials used on an LVDT prototype', *J. of Appl. Research and Tech.*, 2012, **10**, (2), pp. 195-205

[12] Sumali, H., Bystrom, E.P., Krutz, G.W.: 'A displacement sensor for nonmetallic hydraulic cylinders', *IEEE Sen. J.*, 2003, **3**, (6), pp. 818 – 826

[13] Erdelyi, E. A., Ahamed, S. V., Burtness, R. D.: 'Flux distribution in saturated DC machines at no-load', *IEEE Trans. Power App. and Sys.*, 1965, **84** , (5), pp. 375 – 381

[14] Binns, K. J., Lawrenson, P. J.: '*Analysis and computation of electric and magnetic field problems*'(2nd Edition, Pergamon International Library of Science, Technology, Engineering and Social Studies, 1st January 1973)

[15] Nasar, S. A., Boldea, I.: '*Linear motion electric machines*' (John Wiley & Sons Inc; 1st Printing edition, August 1976)

[16] Stoll, R. L.: '*Analysis of eddy currents*'(Clarendon Press, 1974)

[17] Weissinger, C., Oswald, A., Herzog, H.-G.: 'Design of a position sensor using finite-element analysis based on the effect of local magnetic saturation', *IET Sci. Meas. Technol.*, 2012, **6**, (5), pp. 364–368

[18] Yang, S.-H., Hirata, K., Ota, T., et al.: 'Impedance linearity of contactless magnetic-type position sensor', *IEEE Trans. Mag.*, 2017, **53**, (6), pp. 1-4,

[19] Singh, W. S., Mukhopadhyay, C. K., Chandra Rao, B. P.: 'Development of a high sensitive magnetic flux leakage instrument for imaging of localised flaws in small diameter ferromagnetic steel tubes', *IET Sci. Meas. Technol.*, 2018, **12**, (7), pp. 932-936

[20] 'Ansys-Maxwell software', https://www.ansys.com/products/electronics/ansys-maxwell, Accessed on 23.01.2019

[21] Salon, S.: '*Finite element analysis of electrical machines*' (Springer-Verlag (New York) Inc. , 1995)

[22] Ripka, P., Tipek, A.: '*Modern sensors handbook*' (Wiley-ISTE, March 2013)

[23] Clayton, R. P.: '*Inductance: loop and partial*' (Wiley-IEEE Press; 1st edition, Dec 2009)

[24] Ripka, P., Mirzaei, M., Chirtsov, A., Vyhnanek, J.: 'Transformer position sensor for a pneumatic cylinder', Sens. &Act. A, 2019, **294**, pp. 91-101

[25] Talaat, M., Mostafa, N. H.: 'Use of finite element method for the numerical analysis of eddy current brake'. 15th International Workshop on Research and Education in Mechatronics (REM), Elgouna, Egypt, September 9-11, 2014

[26] Talaat, M., Metwally, H. M. B., Arafa, I.: 'Experimental and simulation study of wireless power transfer using resonators with coupled electric fields', *IEEE Trans. Plasma Sci.*, 2018, **46**, (7), pp. 2480-2487

[27] Reinholz, B., Seethaler, R. J.: 'Design and validation of a variable reluctance differential solenoid transducer', *IEEE Sens. J.*, 2019 (Early access)

[28] Grima, A., Castro, M. D., Masi, A., Sammut, N.: 'Design enhancements of an ironless inductive position sensor', *IEEE Trans. Instr. & Meas.*, 2019 (Early access)

[29] Lesniewska, E., Rajchert, R.: 'Behaviour of measuring current transformers with cores composed from different magnetic materials at non-rated loads and overcurrents', *IET Sci. Meas. Technol.*, 2019, **13**, (7), pp. 944–948

[30] Abu-Siada, A., Radwan, I., Abdou, A. F.:'3D approach for fault identification within power transformers using frequency response analysis',*IET Sci. Meas. Technol.*, 2019, **13**, (6), pp. 903–911

[31] Saxena, S. C., Seksena, S. B. L.: 'A self-compensated smart LVDT transducer', *IEEE Trans. Instr.& Meas.*, 1989, 38, (3), pp. 748-753

[32] Bera, S. C., Sarkar, R., Bhowmick, M.: 'Study of a modified differential inductance measurement circuit as position transducer of a power cylinder', *IEEE Trans. Instr. & Meas.*, 2012, **61**, (2), pp. 530-538

[33] Tian, G .Y., Zhao, Z.X., Baines, R.W., Zhang, N.: 'Computational algorithms foe linear variable differential

transformers (LVDTs)', *IEE Proc.-Scie. Meas. Technol.*, 1997, **144**, (4), pp. 189-192
[34] Mishra, S. K., Panda, G., Das, D. P.: 'A novel method of extending the linearity range of linear variable differential transformer using artificial neural network', *IEEE Trans. Instr. & Meas.*, 2010, **59**, (4), pp. 947-953
[35] Yin, S., Ma, X.: 'Analytical model for the equivalent impedances of the domestic induction heating system with rectangular cross-sectional windings', *IET Sci. Meas. Technol.*, 2019, **13**, (7), pp. 1026-1032
[36] Nagel, J. R.: 'Fast Finite-difference calculation of eddy currents in thin metal sheets', *ACES J.*, 2018, **33**, (6), pp. 575-584
[37] Gieras, J. F.:, 'Analytical method of calculating the electromagnetic field and power losses in ferromagnetic halfspace, taking into account saturation and hysteresis', *Proc. of the Inst. of Elec. Eng.*,1977,**124,** (11), pp. 1098 -1104